Three-dimensional multiresonant lossy sonic crystal for broadband acoustic attenuation: Application to train noise reduction

T. Cavalieri [a], A. Cebrecos [a], J.-P. Groby [a], C. Chaufour [b], V. Romero-García [a],*

[a] Laboratoire d'Acoustique de l'Université du Mans, LAUM, UMR CNRS 6613, Av. Olivier Messiaen, Le Mans, France
[b] SNCF, Direction Innovation & Recherche, Av. des Terroirs de France, Paris, France

ARTICLE INFO

ABSTRACT

Broadband acoustic attenuation produced by a three dimensional (3D) locally resonant sonic crystal (LRSC), exploiting both the multiple coupled resonances and the Bragg band gaps, is numerically and experimentally reported in this work. The LRSC is made of square cross-section scatterers arranged on a square lattice and periodically incorporating both quarter-wavelength and Helmholtz resonators along their heights. Local resonators of different types are combined with the periodicity of the system generating multiple coupled resonances at low frequencies and opening Bragg band gaps respectively. This twofold coupling produces a strong broadband attenuation: a large insertion loss (IL), with an average value of 16.8 dB, covering three and a half octaves from 350 Hz to 5000 Hz with a LRSC of 30 cm width. This frequency band corresponds to one of the several railway noise sources (rolling noise, traction auxiliaries, etc.). A simplified 2D LRSC is finally analyzed numerically in a real train-track configuration, showing the efficiency of the proposed design to attenuate the railway rolling noise.

© 2018 Elsevier Ltd. All rights reserved.

1. Introduction

The acoustic properties of locally resonant sonic crystals (LRSC) [1–4] have been extensively exploited over the last years for applications in acoustics based on acoustic filters [5], lenses [6], waveguides [7], energy trapping systems [8] and isolation devices [9], among others. The design of acoustic barriers for environmental noise remains yet the most widespread application [9–21]. LRSC are effectively excellent candidates in a plethora of applications to efficiently attenuate airborne sound thanks to their broadband filtering ability. This ability yields in the coupling of both the periodicity (band gaps) and the coupled local resonances (stop bands), [9,12,13,21]. Moreover, air and light might flow through LRSC, which is particularly suitable in urban contexts. LRSC effectively exhibit a drastic reduction of air flow resistivity when compared to usual sound barriers, which directly implies a reduction of the foundation costs [20].

Environmental noise includes railway noise, which encompasses different kind of noise sources. Railway noise is generally classified in three categories: auxiliary, rolling, and aerodynamic noises. Auxiliary noise arises from the different technical equipments, like diesel engine, power transformer, converter, etc. These equipments are located in the upper or lower parts of locomotives and coaches, either on the roof or at the wheel height. This noise is predominant during parking periods and at very low train speeds ($\leqslant 50$ km.h^{-1}). Rolling noise is radiated by the rolling stock and the track, due to the vibration originated at the wheel-track contact, mostly because of rail roughness and corrugation. The global noise radiation is therefore the sum of different contributions arising from the train wheels, the rail and the sleepers of the track. This second type of noise is predominant for train speeds between 80 and 300 km.h^{-1}. Finally, the aerodynamic noise appears for higher train speeds, up to 300 km.h^{-1}.

In this article, we focus on rolling noise and the design of a LRSC in the corresponding frequency range. The attenuating properties of a 3D LRSC made of square cross-section scatterers arranged on a square lattice and periodically incorporating both quarter-wavelength resonators (QWR) and Helmholtz resonators (HR) along their heights are theoretically and experimentally studied. Viscothermal losses are accounted for both in the QWR and HR by using the Zwikker and Kosten formulae [22,23]. The combination of stop bands, due to local resonant scatterers generating multiple coupled resonances at low frequencies, with bandgaps, due to periodicity, is exploited to produce the broadest and largest possible value of the insertion loss (IL). The HR are deep subwavelength resonators, the resonance of which is in our case $\lambda/l = 18$, where λ is the wavelength and l is the length of the HR. The QWR are

---

designed such that their resonance frequency coincides with the Bragg band gap. Numerical predictions and experimental results show a strong broadband attenuation, the LRSC exhibits a large *IL* covering three and a half octaves with an average value of 16.8 dB from 350 Hz to 5000 Hz. Finally, a simplified 2D LRSC is numerically analyzed in a real train-track configuration, showing the efficiency of the proposed design for the attenuation of rolling noise.

The article is organized as follows. In Section 2 the modeling of both the local resonators and the LRSC is presented. The way the viscothermal losses are accounted for in the local resonators and the conditions used to calculate the dispersion relation and the scattering problem of the 3D LRSC are explicitly presented. Section 3 shows the experimental setup, while the results are discussed in Section 4, also including a simplified 2D LRSC numerically analyzed in a real train-track configuration. Finally, concluding remarks are summarized in Section 5.

2. Modeling

The modeling of the local resonators as well as the whole periodic system, including the scatterers together with the local resonators, are detailed in the following subsections.

2.1. Local lossy resonators

Figs. 1(a) and (b) show the schematics of the QWR and HR, respectively. The QWR consists of a cylindrical borehole carved out of a square-rod scatterer. The HR is composed of a cylindrical neck added to the same cylindrical borehole. The propagation of acoustic plane waves in a circular cross-section duct of radius r_c accounting for the viscothermal losses is described by the complex and frequency dependent effective density and bulk modulus, as described in Ref. [23]

(a) (b)

Quarter-wave   Helmholtz

(c)

(d)
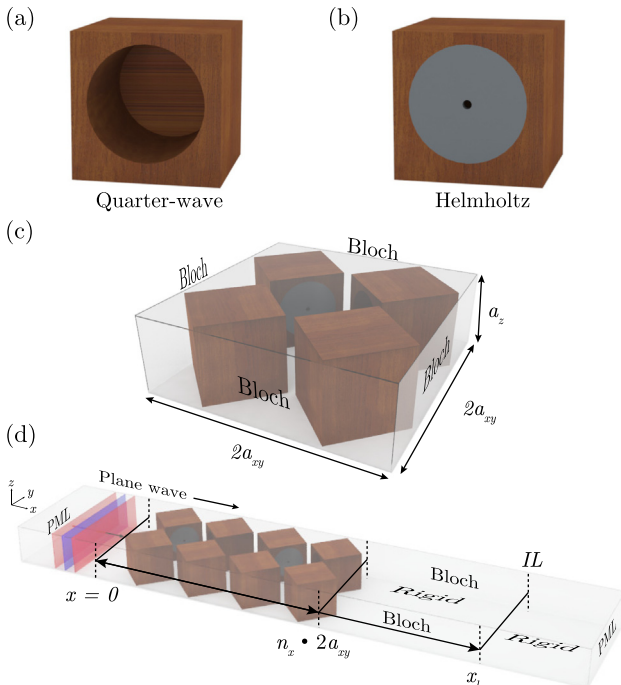
Fig. 1. Schematics of the modeling. Local resonators: (a) Quarter-wavelength and (b) Helmholtz resonators. (c) Three-dimensional unit cell employed for the eigenvalue problem. (d) Scattering problem for the calculation of the IL of an infinite LRSC slab.

$$\tilde{\rho}_c = \rho_0 \left(1 - \frac{2J_1\left(r_c \widetilde{G}_r\right)}{r_c \widetilde{G}_r J_0\left(r_c \widetilde{G}_r\right)} \right)^{-1}, \tag{1}$$

$$\tilde{\kappa}_c = K_0 \left(1 + (\gamma - 1) \frac{2J_1\left(r_c \widetilde{G}_k\right)}{r_c \widetilde{G}_k J_0\left(r_c \widetilde{G}_k\right)} \right)^{-1}, \tag{2}$$

where $\widetilde{G}_r = \sqrt{\iota \omega \rho_0 / \eta}$ and $\widetilde{G}_k = \sqrt{\iota \omega \mathrm{Pr} \rho_0 / \eta}$, with $\iota = \sqrt{-1}$, ρ_0 is the density, $K_0 = \gamma P_0$ is the bulk modulus of air, γ is the specific heat ratio, P_0 is the atmospheric pressure, Pr is the Prandtl number and η is the dynamic viscosity. We notice that the frequency dependent effective properties of more complex geometries have been also obtained in Ref. [23]. Alternatively, we can define the effective impedance $\widetilde{Z}_c = \tilde{\rho}_c \tilde{\kappa}_c$ and wavenumber $\tilde{k}_c = \omega \sqrt{\tilde{\rho}_c / \tilde{\kappa}_c}$ from Eqs. (1) and (2).

Using the effective parameters for a cavity element (Eqs. 1,2), the impedance of a QWR made of a circular borehole of diameter $d_{qwr} = 2r_{qwr}$ (where r_{qwr} is the radius of the borehole) and length l_{qwr} can be written as [24]

$$\widetilde{Z}_{\mathrm{QWR}} = -\iota Z_{qwr} \cot(k_{qwr} l_{qwr}), \tag{3}$$

where Z_{qwr} and k_{qwr} are obtained from Eqs. 1,2.

It is worth noting here that this expression is not exact as long as correction length due to radiation is not included. The characteristic impedance accounting for the borehole radiation can be expressed as [25]:

$$\widetilde{Z}_{\mathrm{QWR}} = -\iota Z_{qwr} \cot(k_{qwr} l_{qwr}) + \iota k_{qwr} \Delta l Z_{qwr}, \tag{4}$$

where the correction length reads as $\Delta l = 0.6 r_c$.

Similarly, the impedance of a HR made of a cylindrical neck of diameter $d_n = 2r_n$ and length l_n, and a cylindrical cavity of diameter $d_c = 2r_c$ and length l_c can be written as [26]

$$\widetilde{Z}_{\mathrm{HR}} = \iota Z_n \frac{A - \tan k_n l_n \tan k_c l_c}{A \tan k_n l_n + \tan k_c l_c}, \tag{5}$$

where $A = Z_c / Z_n$ and k_n (k_c), Z_n (Z_c) are the effective wavenumbers and effective characteristic impedances in the neck (cavity) of the HR.

It is again worth noting here that this expression should account for the radiation of each element. Therefore, the correct expression of the characteristic impedance becomes [26]:

$$\widetilde{Z}_{\mathrm{HR}} = -\iota \frac{c_n c_c - Z_n k_n \Delta l c_n s_c / Z_c - Z_n s_n s_c / Z_c}{s_n c_c / Z_n - k_n \Delta l s_n s_c / Z_c + c_n s_c / Z_c}, \tag{6}$$

where $c_n = \cos(k_n l_n), c_c = \cos(k_c l_c), s_n = \sin(k_n l_n), s_c = \sin(k_c l_c)$. The length correction is deduced from the addition of two correction lengths $\Delta l = \Delta l_1 + \Delta l_2$ respectively defined as $\Delta l_1 = 0.82 \left[1 - 1.35 \frac{r_n}{r_c} + 0.31 \left(\frac{r_n}{r_c} \right)^3 \right] r_n$ and $\Delta l_2 = 0.6 r_n$

The first length correction, Δl_1, is due to pressure radiation at the discontinuity from the neck to the cavity of the HR [27], while the second length correction, Δl_2, comes from the radiation at the discontinuity from the neck to the surrounding medium [28].

2.2. Numerical modeling of the periodic system

We introduce now the numerical models of the LRSC utilized in this work, which are solved using the Finite Element Method (FEM). We first solve an eigenvalue problem to obtain the dispersion relation of an infinite lossless 3D LRSC, and then a scattering problem using two different LRSC slabs, one having an infinite transversal length and the other one a finite length by considering the viscothermal losses in the resonators but not outside the

scatterers. The former represents a case close to a real acoustic barrier of very large transversal length while the latter will serve to compare the attenuation performance with the experimental results measured in an anechoic chamber. For all three cases the spatial domain is discretized creating at least 6 elements per wavelength for the highest analyzed frequency, λ_{min} (6000 Hz, hence $\lambda_{min} = 5.7$ cm).

2.2.1. Eigenvalue problem: dispersion relation

The 3D unit cell of the LRSC used in this study is shown in Fig. 1 (c). It is composed of four scatterers embedding resonators of different type and rotated 45 degrees around their vertical axes with respect to the lattice orientation. All four resonators are facing the center of the unit cell in such a way that identical resonators are facing one with each other, i.e., the two HRs and the two QWRs are in front of each other. This specific orientation of the scatterers arise from the fact that the broadest achievable band gap of a two-dimensional sonic crystal composed of square cross-section scatterers is produced when these are rotated 45 degrees around their axes [29]. In addition, the selected distribution of different types of resonators is obtained from the analysis of different configurations, choosing the one, featuring the broadest stop band, as shown in the Appendix A.

The unit cell shown in Fig. 1(c) is discretized using 4.5×10^4 elements. The boundaries of the wooden square cross-section scatterers are considered acoustically rigid and Floquet-Bloch boundary conditions are assumed on the edges of the unit cell to account for the periodicity of the system (see Fig. 1(c))

$$p\left(\vec{r} + \vec{R}\right) = p(\vec{r})e^{i\vec{k}_B \cdot \vec{R}}, \tag{7}$$

where $\vec{R}$ is the lattice vector and $\vec{k}_B$ is the Bloch vector. By fixing the wavevector, $\vec{k}_B = (k_{Bx}, k_{By}, k_{Bz})$ at a specific location along the path of the irreducible Brillouin zone, the corresponding eigenfrequencies are evaluated, and the dispersion relation of the periodic structure is calculated. In the present case, the irreducible Brillouin zone is not fully representative of the periodic system due to the particular distribution of different resonators in the unit cell. Hence, the main directions of symmetry in the reciprocal space are following the path ΓX - XM - MΓ - ΓM', i.e., considering the ranges $k_{Bx} = [-\pi/2a_{xy}, \pi/2a_{xy}]$ and $k_{By} = [0, \pi/2a_{xy}]$, for $k_{Bz} = 0$.

2.2.2. Scattering problem: infinite LRSC slab

The geometry of the scattering problem using an infinite LRSC slab, i.e. a finite thickness and infinite width system, as it is shown in Fig. 1(d). In the illustrated example, the infinite slab is composed of $n_x = 2$ unit cells along the propagation direction (x-direction, thickness); boundary conditions along the y- and z-directions are chosen such that the structure can be considered periodic along these two directions. A plane wave impinges the structure from the negative x-axis (ΓX direction). Perfectly matched layers (PML) are applied on both ends along the x-direction. The whole solution domain is discretized into 2.2×10^5 elements.

The pressure field is evaluated in the axial plane, i.e., the xy-plane, for $z = a_z/2$. In order to evaluate the attenuation of the 3D LRSC, the IL at frequency f is spatially averaged using M points along a line ranging from $y = [-a_{xy}, a_{xy}]$ behind the LRSC at $x = x_l = 0.65$ m (see Fig. 1(d)).

$$\langle IL(f) \rangle = 20\log_{10}\left(\frac{\sum_{i=1}^{M}|\tilde{p}_{ref}(\vec{r}_i, f)|}{\sum_{i=1}^{M}|\tilde{p}_{sc}(\vec{r}_i, f)|}\right). \tag{8}$$

where $|\tilde{p}_{ref}(\vec{r}, f)|$ and $|\tilde{p}_{sc}(\vec{r}, f)|$ are the absolute values of the acoustic pressure in the absence and in the presence of the 3D LRSC, respectively. It is worth noting here that the length x_l is large enough to

avoid the contribution from evanescent waves scattered by the structure.

2.2.3. Scattering problem: finite LRSC slab

The finite slab is a LRSC with finite thickness and width. In our case we choose $n_x = 2$ unit cells along the x direction (thickness), $n_y = 9$ unit cells along the y direction (width) and of infinite height along the z direction is considered and will be presented later in Section 4. The acoustic source is modeled as a piston of infinite length along the z direction placed at 1.4 m from the structure. Boundary conditions along the z-direction are chosen such that the LRSC can be considered of infinite height. PML layers are considered on both ends on x- and y-directions, hence the only contributions from the incident field behind the LRSC are those propagating through the structure and from its lateral edges. The spatial discretization is performed using $1.85 \ 10^6$ elements.

3. Experimental setup

Our attention is now turned into the description of the experimental setup, introducing the geometry of the locally resonant scatterers, including both types of resonators; the whole periodic system, i.e., the finite LRSC slab and the instrumentation and experimental methods employed for the measurements.

3.1. Locally resonant scatterers

The scatterers consist of wooden rods of square cross-section. Each rod is $0.05 \times 0.05 \times 2.00$ m^3 (i.e., $L = 0.05$ m) and incorporates 29 resonators in its central area along the z-direction separated by a distance $a_z = 0.05$ m. Each QWR has a diameter $d_Q = 0.035$ m and depth $l_Q = 0.04$ m (see Fig. 2(a)). HRs are obtained by inserting a l_n-thick PVC annular disc on top of the QWRs. The inner hole of each PVC annular disc plays the role of the HR neck. The neck diameter is $d_n = 0.004$ m and its length is $l_n = 0.004$ m. The diameter of the HR cavity is $d_c = 0.035$ m and its depth $l_c = 0.036$ m (see Fig. 2(b)).

3.2. Periodic arrangement of locally resonant scatterers: LRSC

The LRSC is composed of an arrangement of locally resonant scatterers, distributed in a 2D square lattice with a lattice period $a_{xy} = 0.075$ m, as shown in Fig. 2(c). The vertical lattice period of the resonators along the scatterer height is $a_z = 0.05$ m. Therefore, the 3D unit cell is a parallelepiped rectangle with a lattice constant $2a_{xy}$, as shown in Fig. 2(d). The LRSC experimentally analyzed is built by using 2 unit cells along the propagation direction, $x-$direction, and 9 unit cells along the transverse direction, $y-$direction. The filling fraction of the LRSC, defined as the ratio of the volume of the scatterers V_{sc} over the total volume of the unit cell V_{cell}, is $ff = \frac{V_{sc}}{V_{cell}} \approx 0.314$. V_{sc} is defined in this work as the solid part of the unit cell.

Experimental measurements are performed using a microphone B&K 1/4" type 4135. The acoustic source is a loudspeaker Genelec 8351A. The excitation signal is a sweep sine function ranging from 50 to 6000 Hz with a step of 12 Hz. The positions of the microphone along the measurement line are controlled by a Zaber LSQ 1D robotized arm. The acquisition of the acoustic signal is performed using a Stanford SR 785 spectrum analyzer. A picture of the experimental setup is represented in Fig. 2(e). The loudspeaker used to generate the acoustic field in the anechoic chamber is placed at an approximate distance of 1.4 m from the LRSC. A single microphone is utilized to measure the transfer functions between the electrical and the acoustic signal measured at every point along the line behind the LRSC. Only propagation along the $x - y$ plane is considered.
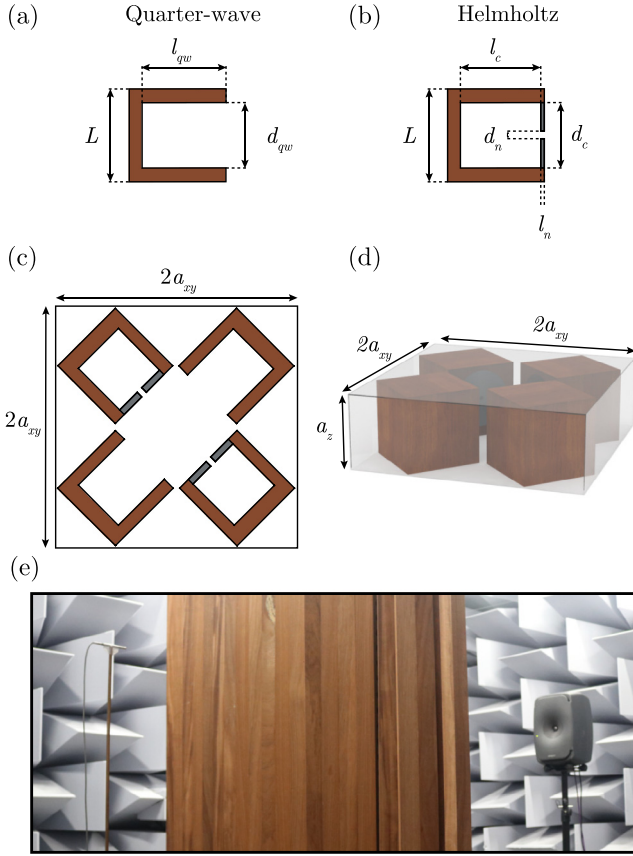
Fig. 2. Experimental set-up. (a), (b) Transversal views of both types of resonators, QWR and HR, respectively. (c), (d) Schematic diagram of the unit cell and main geometrical parameters. (e) Picture of the experimental set-up in the anechoic chamber.

3.3. Insertion Loss

The attenuation of the LRSC is evaluated measuring the *IL* along a line behind the sample at $x_l = 0.65$ m, ($x = 0$ is located following the same convention presented in Fig. 1(d)). This measurement line spans the interval $y_l = [-0.225, 0.225]$ cm with 1 cm step ($M = 46$ points). The transfer function between the signal registered by the microphone and the input electrical signal is measured twice along this line, i.e., in the absence and in the presence of the LRSC, and later spatially averaged. The absolute value of the spatially averaged complex transfer function at point $\vec{r}_i$ and frequency f is given by

$$\left\langle |\widetilde{H}(f)| \right\rangle = 20\log_{10}\left(\frac{1}{M|\widetilde{V}(f)|} \sum_{i=1}^{M} |\tilde{p}(\vec{r}_i, f)| \right), \qquad (9)$$

where $\widetilde{H} = \left(\widetilde{H}_{ref}, \widetilde{H}_{sc} \right)$, and $\tilde{p} = (\tilde{p}_{ref}, \tilde{p}_{sc})$ is the measured acoustic pressure along the line. Note that subscripts refer to measurements performed in the absence and in the presence of the LRSC. The spatially averaged $\langle IL \rangle$ is obtained making use of Eq. (8).

4. Results

4.1. Characterization of the local lossy resonators

The local resonators used in the LRSC are characterized in this subsection. A numerical full wave simulation mimicking an impedance tube measurement is performed in order to obtain the acoustic impedance of the local resonators. The configurations of

the impedance tube considered for the QWR and HR are shown in Figs. 3(a, b), respectively. To characterize the acoustic properties of the local resonators, the effective properties given by Eqs. 1,2 are introduced in their respective domains. The acoustic impedance of each resonator is recovered from the numerical model evaluating the transfer function, and compared to the analytical expressions given by the Eqs. (4, 6). Note that the previous analytical models have been already validated experimentally [30,31].

Figs. 3(c, d) show the real and imaginary part of the normalized impedance of the QWR and HR, respectively. Continuous and dashed lines correspond to analytical predictions from Eqs. (4, 6), while symbols represent results from the numerical model presented previously. Numerical and analytical results are in excellent agreement, which validate the model used in this work to account for the losses. Note that viscothermal losses are considered in both calculations, hence the value of the resonance frequency represents the behavior of the resonator itself, with no coupling to other resonant elements. The resonance frequency corresponds to the frequency at which $\Im\left(\widetilde{Z}_{res} \right) = 0$ (where *res* =QWR, HR). By doing so, the resonance frequency of the HR is found at $f_{HR} = 380$ Hz and that of the QWR at $f_{QWR} = 2000$ Hz.

4.2. Locally resonant sonic crystal

4.2.1. Dispersion relation

The dispersion relation along the main directions of symmetry (ΓX-XM-MΓ-ΓM') for the unit cell described in Section 2 is shown in Fig. 4(a). The several bands shown in the dispersion relation are due to the folding effect related to the supercell behaviour of the structure. At low frequencies (around 400 Hz) a full stop band is observed due to the resonance of the HRs. The pressure distribution of the unit cell (eigenvector) at the resonance frequency of the HR corresponding to point X of the dispersion relation is shown in Fig. 4(b). At this frequency, the pressure field is mostly located in the HR. For higher frequencies, but still lower than the Bragg band gap which is around 2200 Hz, other pseudo-band gaps are opened in the ΓX direction as a consequence of additional cavity mode excitation [21]. For example, the pressure distribution at frequency 1190 Hz at point Γ is shown in Fig. 4(c), for which a cavity mode in the external cavities of the unit cell is well activated creating a
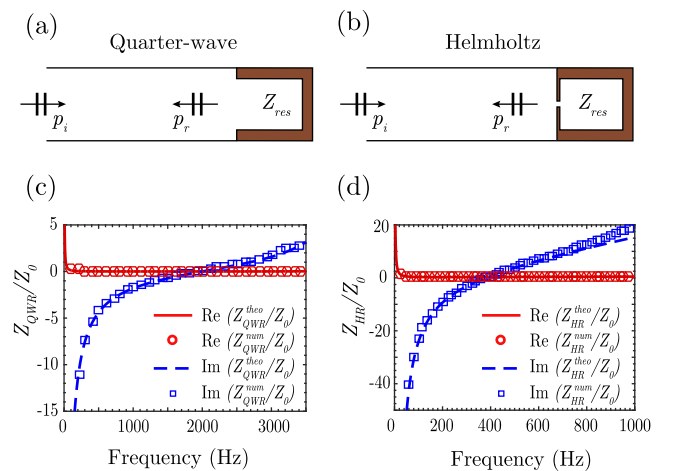
Fig. 3. Characterization of the local resonators, comparison between analytical and numerical results. (a), (b) show configurations in an impedance tube with QWR and HR, respectively. Real (red continuous line for analytics and red open circles for numerics) and imaginary (blue dashed line for analytics and blue open squares for numerics) parts of the normalized acoustic impedance of the (c) QWR, Z_{QWR}/Z_0 and (d) HR, Z_{HR}/Z_0. (For interpretation of the references to colour in this figure legend, the reader is referred to the web version of this article.)
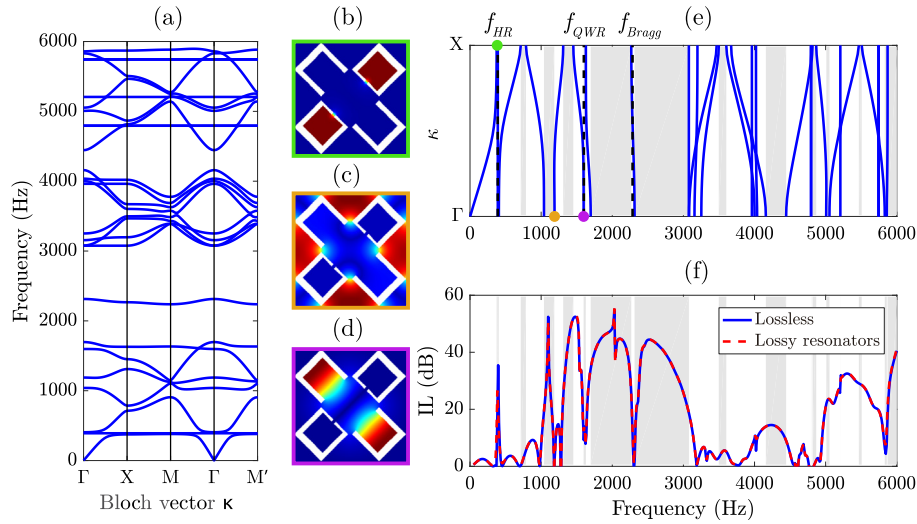
Fig. 4. Numerical characterization of the LRSC. (a) Dispersion relation along the main symmetry directions. Eigenvectors at particular frequencies: (b) resonance frequency of the HR, f_{HR} = 390 Hz, (c) additional cavity modes at 1190 Hz, (d) resonance frequency of the QWR, f_{QWR} = 1600 Hz. (e) Dispersion relation along the ΓX direction. (f) Numerical IL for an infinite LRSC slab.

band gap around this frequency in the ΓX direction. Finally, we show the eigenvector at frequency 1600 Hz at point Γ (see Fig. 4 (d)). At this frequency, the coupled QWRs open another stop band, as shown in Fig. 4(e). At higher frequencies, the combined effects of the QWRs and the periodicity produce a full band gap between 1600 Hz and 3000 Hz. Higher band gaps can be also observed in the dispersion relation due to periodicity and higher order resonant modes.

4.2.2. IL of an infinite LRSC slab

To analyze in detail the effect of the HR, the QWR and periodicity, the dispersion relation along the ΓX direction shown in Fig. 4 (e) is compared to the IL produced by an infinite LRSC slab composed of n_x = 2 unit cells. The IL produced by this infinite slab is shown in Fig. 4(f) for the lossless (blue continuous line) and the lossy (red dashed line) cases. The attenuation peaks observed in the IL spectrum are in very good agreement with the band gaps obtained from the eigenvalue problem. At the resonant frequency of the HR, f_{HR} = 390 Hz, we observe an IL peak of amplitude 35 dB. Interestingly, for higher frequencies the coupling of the QWR and the effect of periodicity produces IL peaks of amplitude 40 dB. Note that the losses are only accounted for in the resonators, therefore their main effects are manifested at their resonance frequencies. The influence of losses in the case of the HR is significant, producing an impedance mismatch and therefore a reduction of the IL peak at 390 Hz. For the QWR, the effects of losses are mostly negligible.

The analysis of an infinite LRSC slab is of large importance to have an idea of the effect of a large barrier, as it would be the case for an application in the context of railway noise control. However, in many practical situations, and in particular for this work, the experimental analysis is performed in an anechoic chamber using a structure of finite transversal length. Hence the interference pattern produced by both edges of the structure should be accounted for in the numerical simulations, as shown in the next Section.

4.2.3. IL of a finite LRSC slab

The schematic diagram of the finite LRSC slab used for the corresponding numerical calculations is shown in Fig. 5(a), where IL is evaluated following the same exact procedure described in Section 3.3. Numerical (blue continuous and red dashed lines for the lossless and lossy cases, respectively) and experimental (gray circles) IL results for a finite LRSC slab show a very good agreement, as shown in Fig. 5(b). The finite size effect of the structure strongly affects the amplitude of the IL peaks in comparison with the infinite slab, reducing the attenuation of the structure. However, the frequencies of the IL peaks present the same behavior as those of the infinite slab (see Fig. 4(f)). We notice that between 3000 Hz and 5000 Hz the experimental results show better IL than the analytical model. This is due to the fact that losses are not accounted for out of the resonators and, therefore, in this range of frequencies the scattering is the most important phenomenon. However, our numerical model still captures the trends of the experimental results.

In order to analyze the attenuation ability of the LRSC as an acoustic barrier we have also calculated IL in thirds of octave. Bars in the background of Fig. 5(b) represent the corresponding experimental (grey) and numerical (red) IL values. Results show that the proposed structure increases the attenuation for all the bands between 50 and 6000 Hz. In particular, an overall IL of 16 dB is produced in the range of frequencies of interest, i.e., from 350 to 6000 Hz.
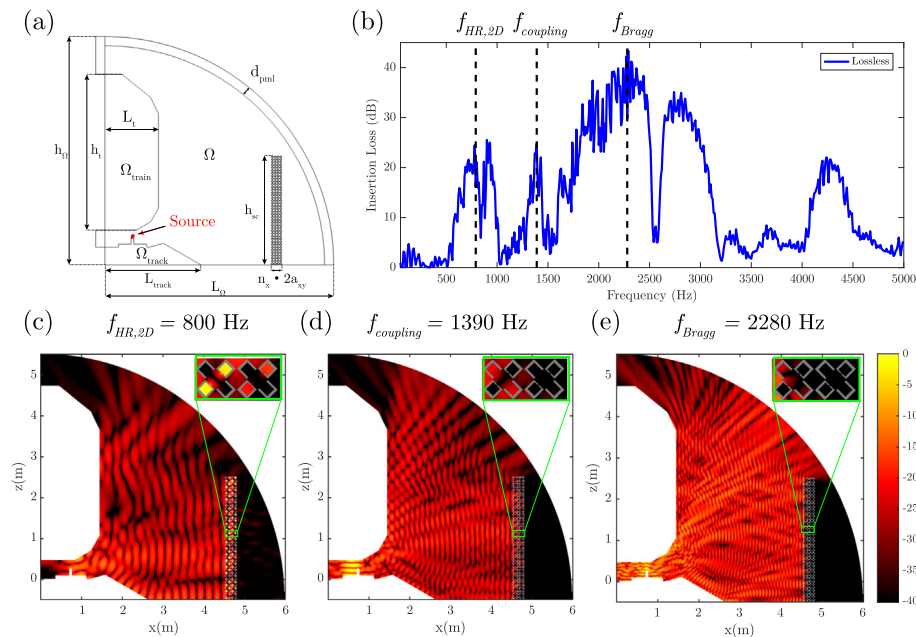
4.3. Simplified model in a real train-track configuration

In this Section we apply a simplified 2D model of the LRSC designed in this work to a realistic case of railway rolling noise application. The geometry is shown in Fig. 6(a). The boundaries of the train and the ground (ballast, sleepers, rail, etc.) are all considered acoustically rigid while the remaining boundaries are modeled adding PML layers. The spatial domain is discretized into 2.3×10^6 elements. The acoustic source is modeled as a point source located at the position of the train wheel.

Fig. 6(b) illustrates numerical IL results, which are spatially averaged along a human-sized vertical line (chosen to be 1.75 m high) located 1 m behind the LRSC. Frequency dependent results present a similar trend to the previous 3D analysis, but in this case the effect of the multiple virtual sources, due to the rigid boundary conditions in the domain, is observable. Three IL snapshots show the sound pressure level maps at three frequencies of interest. At the HR resonance frequency, Fig. 6(c), the omnidirectional effect of the stop band is represented by a strong attenuation of the acoustic field behind the structure. The effect of the ground [32] and reflections produced by the rigid boundary conditions of the
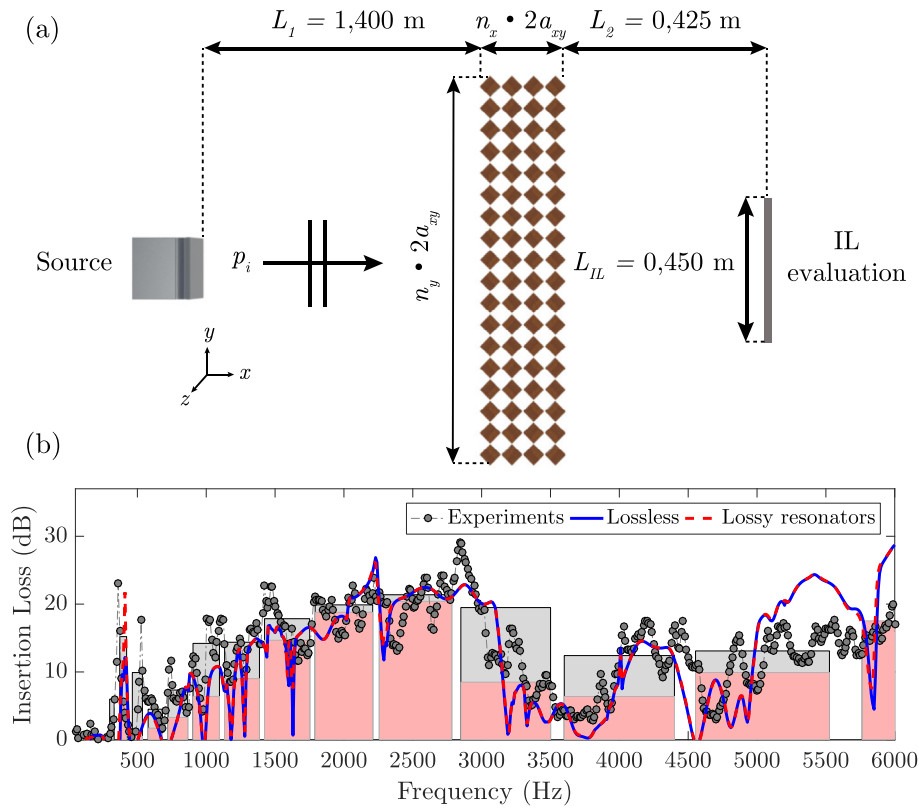
Fig. 5. (a) Schematic diagram of the finite LRSC slab used for numerical simulations. (b) Comparison of the *IL* calculated numerically, with (red dashed line) and without (blue continuous line) losses, and experimentally measured (grey circles). Bars represent *IL* in thirds of octave for the numerical case with losses (red bars) and experiments (grey bars). (For interpretation of the references to colour in this figure legend, the reader is referred to the web version of this article.)

Fig. 6. Simplified 2D model in a real train-track configuration. (a) Geometry of the numerical model. (b) Spatially averaged *IL* results measured along a vertical line behind the LRSC. Acoustic pressure level (in dB) in the domain at three frequencies of interest: (c) Resonance of the HR in 2D, f_{HR} = 800 Hz, (d) Coupling between the QWR, $f_{coupling}$ = 1390 Hz, and (e) Bragg frequency, f_{Bragg} = 2280 Hz.

walls of the train and the ground are strongly attenuated by the crystal, creating an acoustic shadow region behind the LRSC. At higher frequencies, at $f_{coupling}$ = 1390 Hz, Fig. 6(d) shows how the

coupling of the QWR attenuate the incident wave on the LRSC. Finally, at the Bragg frequency, shown in Fig. 6(e), the band gap is producing a strong attenuation in the region under analysis.
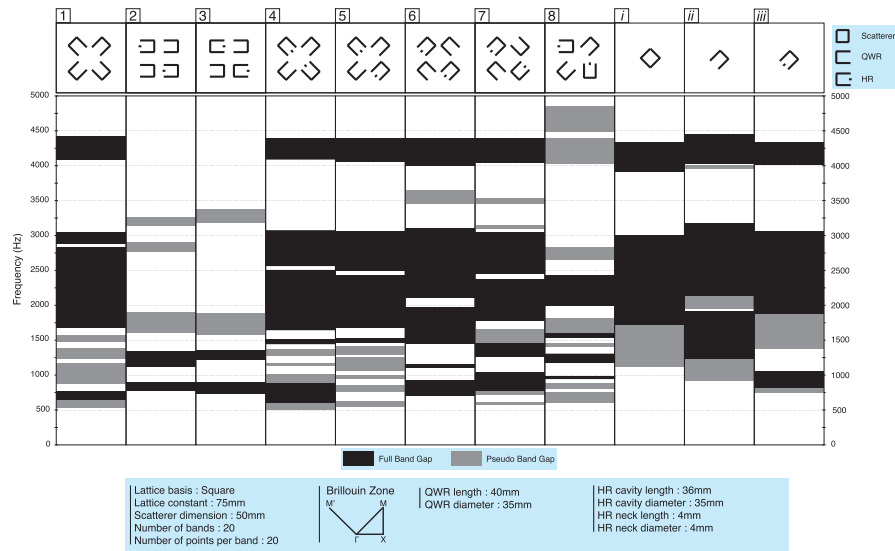
Fig. 7. Preliminary studies of multiple LRSC unit cells. Pseudo band gaps (ΓX), in grey, and full band gaps, in black, for multiple coupling configurations of the LRSC. The frequency range spans from 0 Hz to 5000 Hz. Columns (1) to (8) represent $2a_{xy} \times 2a_{xy}$ supercells, while (i), (ii) and (iii) represent $a_{xy} \times a_{xy}$ unit cells. The configuration shown in column (4) is the one employed throughout this work as it predicts the largest band gaps in the frequency range of interest.

5. Conclusions

A LRSC made of square rod scatterers with embedded HR and QWR is theoretically and experimentally analyzed in this work. The system is designed to work in the range of frequencies corresponding to various railway noise sources, in particular for the case of rolling noise. We exploit the idea of combining local resonators to generate multiple coupled resonances at low frequencies with Bragg band gaps arising from periodicity. We have considered both the viscothermal losses and the finite-size effects of the structure. Viscothermal losses affect the resonators efficiency at their resonances and are negligible for other frequencies. The effect of the transversal length of the structure strongly affects the *IL* peak amplitudes. In the case analyzed in this article, a LRSC of 30 cm width, strong broadband attenuation is obtained: the structure exhibits a large *IL* covering three and a half octaves with an average value of 16.8 dB ranging from 350 Hz to 5000 Hz. These values can be greatly improved in real situations where larger structures of the same thickness can be built. We finally employ the LRSC in a simplified 2D geometry to analyze numerically the attenuation capabilities of the system in a real train-track configuration. The good efficiency of the proposed design to attenuate railway rolling noise opens new routes for designing efficient systems, with unprecedented advantages for increasing the attenuation. Moreover, low flow resistivity and allowing the light to pass through the crystal ensures suitability of the proposed structure for urban contexts.

Appendix A. Appendix

The best combination of HR and QWR is chosen after evaluating the dispersion relations of multiple possible 2D combinations. Fig. 7 illustrates full and pseudo band gaps along the ΓX direction for several combinations.

References

[1] Bradley CE, Acoustic bloch wave propagation in a periodic waveguide, Tech. rep., Technical Report of Applied Research Laboratories, Report No. ARL-TR-91-19 (July), The University of Texas at Austin; 1991.
[2] Sugimoto N, Horioka T. Dispersion characteristics of sound waves in a tunnel with an array of helmholtz resonators. J Acoust Soc Am 1995;97:1446.
[3] Liu Z, Zhang X, Mao Y, Zhu Y, Yang Z, Chan C, Sheng P. Locally resonant sonic materials. Science 2000;289:1734.
[4] Fang N, Xi D, Xu J, Ambati M, Srituravanich W, Sun C, Zhang X. Ultrasonic metamaterials with negative modulus. Nat Mater 2006;5:452–6.
[5] Hu X, Chan CT. Two-dimensional sonic crystals with helmholtz resonators. Phys Rev E 2005;71:055601(R).
[6] Lemoult F, Lerosey G, de Rosny J, Fink M. Resonant metalenses for breaking the diffraction barrier. Phys Rev Lett 2010;104:203901.
[7] Lemoult F, Kaina N, Fink M, Lerosey G. Soda cans metamaterial: a subwavelength-scaled phononic crystal. Crystals 2016;6(7):82.
[8] Lemoult F, Fink M, Lerosey G. Acoustic resonators for far-field control of sound on a subwavelength scale. Phys Rev Lett 2011;107:064301.
[9] Romero-Garća V, Krynkin A, Garcia-Raffi L, Umnova O, Sánchez-Pérez J. Multi-resonant scatterers in sonic crystals: locally multi-resonant acoustic metamaterial. J Sound Vib 2013;332(1):184.
[10] Sánchez-Pérez J, Rubio C, Martínez-Sala R, Sánchez-Grandia R, Gómez V. Acoustic barriers based on periodic arrays of scatterers. Appl Phys Lett 2002;81:5240.
[11] Martńez-Sala R, Rubio C, Garcia-Raffi L, Sánchez-Pérez J, Sánchez-Pérez E, Llinares J. Control of noise by trees arranged like sonic crystals. J Sound Vib 2006;291:100.
[12] Romero-Garća V, Sánchez-Pérez JV, Garcia-Raffi LM. Tunable wideband bandstop acoustic filter based on two-dimensional multiphysical phenomena periodic systems. J Appl Phys 2011;110:149041–9.
[13] Lagarrigue C, Groby JP, Tournat V. Sustainable sonic crystal made of resonating bamboo rods. J Acoust Soc Am 2013;133(1):247.
[14] Krynkin A, Umnova O, Chong AYB, Taherzadeh S, Attenborough K. Predictions and measurements of sound transmission through a periodic array of elastic shells in air. J Acoust Soc Am 2010;128(6):3496–506. https://doi.org/10.1121/1.3506342.
[15] Koussa F, Defrance J, Jean P, Blanc-Benon P. Acoustical efficiency of a sonic crystal assisted noise barrier. Acta Acust United Acust 2013;99(3):399–409.
[16] Castiñeira-Ibáñez S, Romero-Garća V, Sánchez-Pérez JV, Garcia-Raffi LM. Overlapping of acoustic bandgaps using fractal geometries. EPL 2010;92:24007.
[17] Sánchez-Dehesa J, Garća-Chocano V, Torrent D, Cervera F, Cabrera S, Simon F. Noise control by sonic crystal barriers made of recycled materials. J. Acoust. Soc. Am. 2011;129 [1173].
[18] Garća-Chocano V, Cabrera S, Sánchez-Dehesa J. Broadband sound absorption by lattices of microperforated cylindical shells. Appl Phys Lett 2012;101(18):184101.
[19] Garća-Chocano V, Sánchez-Dehesa J. Optimum attenuation of broadband noise by sonic crystals made of recycled materials. Appl Acoust 2013;74:58.
[20] Castiñeira-Ibáñez S, Rubio C, Sánchez-Pérez J. Environmental noise control during its transmission phase to protect buildings. design model for acoustic barriers based on arrays of isolated scatterers. Build Environ 2015;93:179.
[21] Lardeau A, Groby J, Romero-Garća V. Broadband transmission loss using the overlap of resonances in 3d sonic crystals. Crystals 2015;6(5):51.
[22] Zwikker C, Kosten C. Sound Absorbing Materials. Elsevier Publishing Company; 1949.
[23] Stinson MR. The propagation of plane sound waves in narrow, and wide circular tubes and generalization to uniform tubes of arbitrary cross sectional shape. J Acoust Soc Am 1991;89(2):550–8. https://doi.org/10.1121/1.400379.

[24] Schwan L, Geslain A, Romero-Garća V, Groby J-P. Complex dispersion relation of surface acoustic waves at a lossy metasurface. Appl Phys Lett 2017;110 (5):051902. https://doi.org/10.1063/1.4975120.

[25] Kinsler L, Frey AR, Coppens A, Sanders JV. Fundamentals of acoustics. 4th. Ed. New York: John Wiley and Sonc Inc; 2000.

[26] Romero-Garća V, Theocharis G, Richoux O, Pagneux V. Use of complex frequency plane to design broadband and sub-wavelength absorbers. J Acoust Soc Am 2016;139:3395.

[27] Kergomard J, Garcia A. Simple discontinuities in acoustic waveguide at low frequencies: Critical analysis and formulae. J Sound Vib 1987;114(3):465.

[28] Dubos V, Kergomard J, Khettabi A, Dalmont JP, Keefe DH, Nederveen CJ. Theory of sound propagation in a duct with a branched tube using modal decomposition. Acta Acust United Acust 1999;85(2):153–69.

[29] Goffaux C, Vigneron JP. Theoretical study of a tunable phononic band gap system. Phys Rev B 2001;64:075118.

[30] Jiménez N, Huang W, Romero-Garća V, Pagneux V, Groby J-P. Ultra-thin metamaterial for perfect and quasi-omnidirectional sound absorption. Appl Phys Lett 2016;109(12):121902. https://doi.org/10.1063/1.4962328.

[31] Jiménez N, Romero-Garća V, Pagneux V, Groby J-P. Rainbow-trapping absorbers: broadband, perfect and asymmetric sound absorption by subwavelength panels for transmission problems. Sci Rep 2017;7(1):13595. https://doi.org/10.1038/s41598-017-13706-4.

[32] Romero-García V, Sánchez- Pérez JV, Garcia-Raffi LM. Analysis of the wave propagation properties of a periodic array of rigid cylinders perpendicular to a finite impedance surface. EPL 2011;96:44003. https://doi.org/10.1209/0295-5075/96/44003.